Boundary Layers and Material Deformation in Fiber Drawing

John Abbott (Corning Incorporated)
David Ambrose (Duke University)
Richard Braun (University of Delaware)
Cynthia DeBisschop (Old Dominion University)
Pierre Gremaud (North Carolina State University)
Peter Howell (University of Oxford)
Peter Kramer (Rensselaer Polytechnic Institute)
Colin Please (University of Southampton)
Jose Domingo Salazar Gonzalez (University of Oxford)
Donald Schwendeman (Rensselaer Polytechnic Institute)

June 18, 2002

Abstract

We study two fluid dynamical issues which are important in the manufacture of thin glass fibers for communication networks and materials. Such thin fibers are obtained by rapidly pulling molten glass through an array of successively smaller holes. Through asymptotic analysis and physical modeling, we obtain a quantitative description of the flow and structure of the glass fiber as it is being pulled. We examine in particular the issue of whether initially planar cross sections remain planar, and find that they do so approximately, but not exactly, even in the absence of such factors as gravity, surface tension, and inertia. We also develop a quantitative theory for the structure of the air flow near the fiber, which is an important ingredient in determining how fast the fiber cools. In particular, we develop a description for the structure of the boundary layer near a fiber which has accelerating surface velocity and shrinking radius which is comparable or thin compared with the thickness of the boundary layer. One novel feature is that the accleration of the fiber surface velocity leads to a compression of the boundary layer as it evolves downstream.

1 Introduction and Overview

Thin glass fibers, with diameters on the order of tens of microns, are crucial materials for high-speed communication [2, 8] and reinforcement of structural plastic and fabric materials [11]. These fibers are typically manufactured through melting the glass, then drawing it at high speed through a series of holes in "bushing plates" until it reaches its desired radius [11]. A cartoon of the process is depicted in Figure 1. Preform molten glass is supplied from the top through a nozzle of radius H_0, and is pulled by a downward force through a much smaller hole of radius H_1 into a tube in which the glass cools and solidifies into a hopefully uniform fiber. The emerging fiber is pulled at a high speed U_1, and the distance between the nozzle and final bushing plate is denoted by length L; typical values for these fundamental geometric parameters are given in Table 1.

Table 1: Approximate values of physical parameters [2, 8, 11]

Initial nozzle radius	$H_0 \approx$ 1–10 mm,
Final fiber radius	$H_1 \approx$ 5–50 μm,
Length of neck-down region	$L \approx$ 1–2 m,
Final fiber speed	$U_1 \approx$ 15–90 m/s,

In the workshop, we have analyzed two elements of this process which may help inform improvements in the procedure. First, we have studied how the molten glass fiber deforms in the neck-down region in Figure 1. We develop in §2 a mathematical theory to describe its shape and the internal distortion within the fiber. In particular, we have examined whether initially planar cross sections at the upper nozzle remain planar further downstream. That is, suppose at an instant of time we dye a cross section of the fiber that is just emerging from the nozzle. The question is whether this dyed region will remain planar or will buckle as the fiber is drawn down to smaller radius. We find that the thickness of the fiber decays according to an exponential law in the neck-down region, and that planar sections do remain approximately, but not exactly, planar. Numerical simulations have previously been performed to study this issue [2], finding similar results, but the present work provides a mathematical theory which indicates in a quantitative fashion how the fiber shape and distortion and depend on the various physical parameters. Moreover, our analysis shows that the buckling of cross sections of the fiber results simply from dynamical interaction with the evolving free surface. Other factors, such as surface tension, inertia, gravity, temperature-dependent viscosity, and radial temperature gradients can also influence the internal distortion of the fiber, but there is also a basic distortion which cannot be attributed to any of these.

The second contribution from the workshop is the development of some basic theory for the air flow near the fiber. This "boundary layer" air flow arises from the transfer of momentum from the fiber to the air through viscous coupling. Because the fiber is

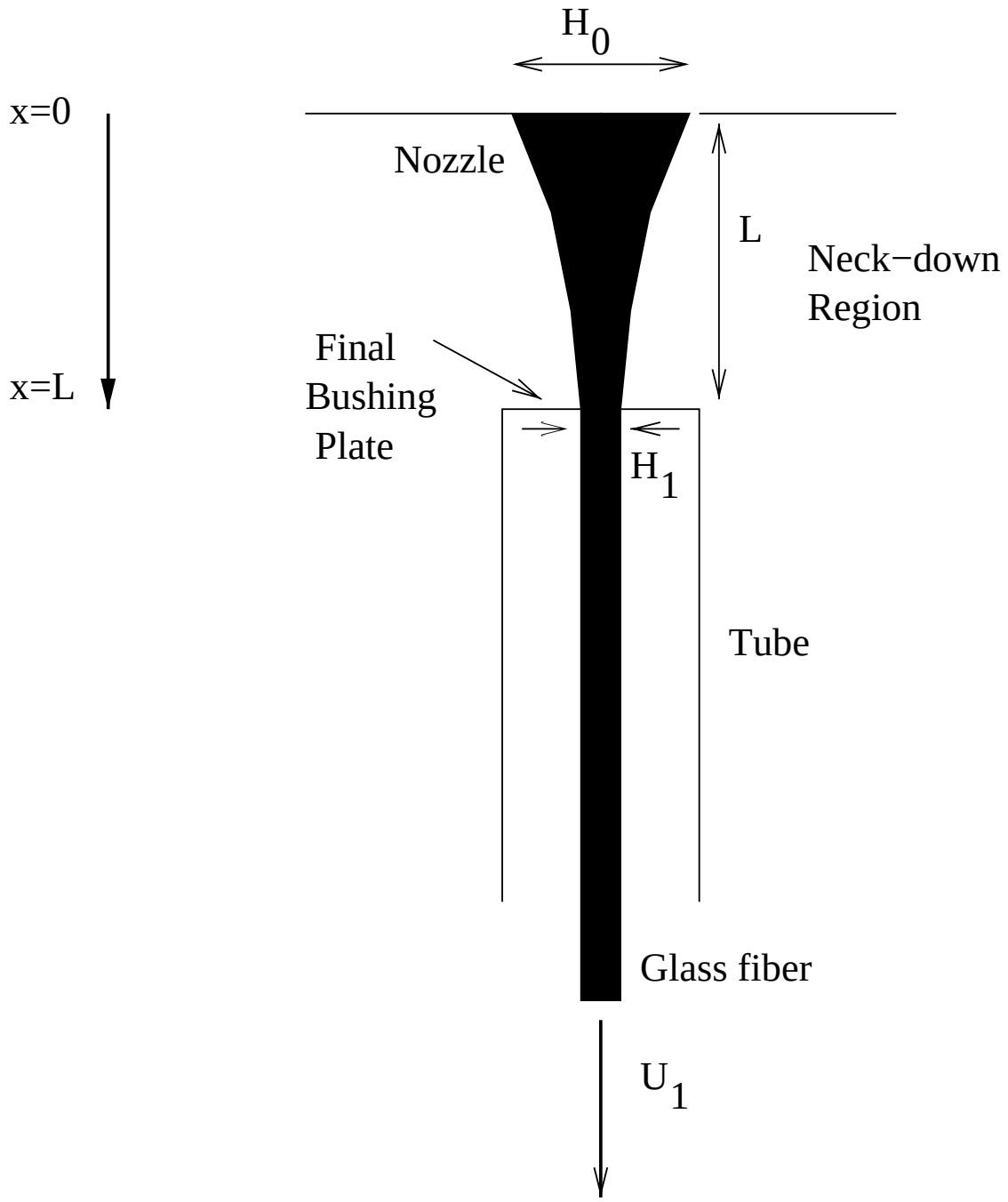

Figure 1: Schematic diagram of process of drawing glass fibers. Figure is not drawn to scale; the fiber is in reality much thinner and the neck-down region much longer; see Table 1.

accelerated to high speed, this air flow can become significant and will affect the rate of heat transfer away from the hot glass into the surrounding atmosphere. In practice, one would like to make this heat transfer very rapid, so that the thinly drawn glass fiber can cool and solidify within a reasonably short distance. By better understanding how the air flow depends on the physical parameters in the glass drawing process, one may be able to design ways to draw the glass so that the cooling region can be made shorter.

Our boundary layer analysis borrows from the vast field of theory from fluid mechanics [4], but the standard theory requires some adaptation to the present application. First of all, in the neck-down region, the fiber surface is rapidly accelerating as the fiber is stretched into a smaller radius. Most boundary layer theory has been developed for fluids flowing past boundaries which are rigid or at least moving with constant speed. Recent work [1] has considered self-similar profiles of the air velocity in the boundary layer near a *flat* stretching surface such that the surface velocity grows according to a power law. Such flat surface analysis would be applicable for a situation in which the boundary layer was thin compared to the radius of curvature of the fiber. Some simple estimates presented in §3.1, based on integrated forms of the momentum equation, indicate however that the boundary layer thickness for the typical data listed in Table 1 will be at least as large as the radius of the fiber. Consequently, we develop a theory for the boundary layer in the neck-down region which is appropriate to situations where the boundary layer can be comparable or larger than the radius of the fiber, though we still assume that the longitudinal (streamwise) radius of curvature is large compared to the boundary layer thickness. This assumption is shown to be consistent with the data in Table 1. Our approach follows the classical path of searching for similarity solutions [4]. It turns out that the most interesting fiber shape for which we can find a nontrivial similarity solution is precisely the one which is predicted by the theory in §2!

Another boundary layer analysis is developed for the air flow in the tube after the fiber has been drawn through the final bushing plate. Here, the complication is the presence of the confining tube, which necessitates some return flow counter to the direction of the fiber motion. In §4, we present a quantitative theory for the air flow throughout this tube, using the method of similarity solutions, matched asymptotic expansions, and integral balance ideas.

Concluding remarks and suggestions for future developments are offered in §5.

2 Quasi-one-dimensional model for a slender viscous fiber

2.1 Governing equations

Consider an axisymmetric fiber of viscous liquid emerging from a nozzle at speed U_0 and being drawn downwards at speed $U_1 > U_0$ a distance L downstream. We model the

liquid as Newtonian, but with a nonuniform viscosity μ, since the viscosity of glass is very strongly dependent on temperature. In terms of cylindrical polar coordinates (x, r) (measuring, respectively, distance along and distance from the fiber axis) with velocity components (u, v) and pressure p, the stress tensor therefore has components

$$\begin{aligned}
\sigma_{xx} &= -p + 2\mu\frac{\partial u}{\partial x}, && (1)\\
\sigma_{rr} &= -p + 2\mu\frac{\partial v}{\partial r}, && (2)\\
\sigma_{\theta\theta} &= -p + 2\mu\frac{v}{r}, && (3)\\
\sigma_{xr} &= \mu\left(\frac{\partial u}{\partial r} + \frac{\partial v}{\partial x}\right), && (4)\\
\sigma_{x\theta} = \sigma_{r\theta} &= 0. && (5)
\end{aligned}$$

In terms of these, the steady Navier-Stokes equations governing the flow of liquid in the fiber may be written as

$$\begin{aligned}
\frac{\partial(ru)}{\partial x} + \frac{\partial(rv)}{\partial r} &= 0, && (6)\\
\frac{\partial(r\sigma_{xx})}{\partial x} + \frac{\partial(r\sigma_{xr})}{\partial r} + \rho g r &= \rho r\left(u\frac{\partial u}{\partial x} + v\frac{\partial u}{\partial r}\right), && (7)\\
\frac{\partial(r\sigma_{xr})}{\partial x} + \frac{\partial(r\sigma_{rr})}{\partial r} - \sigma_{\theta\theta} &= \rho r\left(u\frac{\partial v}{\partial x} + v\frac{\partial v}{\partial r}\right), && (8)
\end{aligned}$$

where ρ is the liquid density and g the acceleration due to gravity.

We describe the free surface of the fiber by $r = h(x)$. On this surface we apply the kinematic boundary condition and dynamic conditions that balance viscous traction with that due to the surface tension γ:

$$\left.\begin{aligned}
v &= uh'(x)\\
\sigma_{xr} &= h'(x)\left(\sigma_{xx} + \gamma\kappa\right)\\
\sigma_{rr} + \gamma\kappa &= h'(x)\sigma_{xr}
\end{aligned}\right\} \text{ on } r = h(x), \qquad (9)$$

where

$$\kappa = \frac{1}{h(x)\sqrt{1 + h'(x)^2}} - \frac{h''(x)}{\left(1 + h'(x)^2\right)^{3/2}} \qquad (10)$$

is the curvature of the free surface. On the axis of the fiber we have to impose conditions of continuity, namely

$$v = \frac{\partial u}{\partial r} = 0 \text{ on } r = 0. \qquad (11)$$

At the ends of the fiber, we specify the velocity, while the fiber radius is prescribed only at the top, because of the kinematic condition (9a):

$$u = U_0, \quad v = 0, \quad h = H_0 \quad \text{at } x = 0, \tag{12}$$

$$u = U_1, \quad v = 0 \quad \text{at } x = L. \tag{13}$$

If the viscosity $\mu(x, r)$ is given, or found *e.g.* by solving a coupled heat-transfer problem, then these equations and boundary conditions comprise a closed problem that determines the shape of the fiber and the velocity and stress fields inside.

2.2 Nondimensionalisation

We rescale the equations and boundary conditions as follows

$$x = L\tilde{x}, \quad r = H_0\tilde{r}, \quad u = U_0\tilde{u}, \quad v = \frac{H_0 U_0}{L}\tilde{v},$$

$$\mu = M\tilde{\mu}, \quad p = \frac{MU_0}{L}\tilde{p}, \quad h = H_0\tilde{h}, \quad \kappa = \frac{1}{H_0}\tilde{\kappa},$$

$$(\sigma_{xx}, \sigma_{rr}, \sigma_{\theta\theta}) = \frac{MU_0}{L}\left(\tilde{\sigma}_{xx}, \tilde{\sigma}_{rr}, \tilde{\sigma}_{\theta\theta}\right), \quad \sigma_{xr} = \frac{MU_0}{H_0}\tilde{\sigma}_{xr}.$$

Notice that the two different lengthscales L and H_0 are used to nondimensionalise x and r, and that M is used to denote a typical viscosity.

There are five dimensionless parameters in the problem. The inverse aspect ratio,

$$\epsilon = \frac{H_0}{L}, \tag{14}$$

measures the slenderness of the fiber, while the draw ratio is the ratio between the nozzle and draw velocities:

$$\mathrm{D} = \frac{U_1}{U_0}. \tag{15}$$

The Reynolds, Stokes and inverse reduced capillary numbers,

$$\mathrm{R} = \frac{\rho U_0 L}{M}, \quad \mathrm{S} = \frac{\rho g L^2}{MU_0}, \quad \mathrm{C} = \frac{\gamma L}{MUH_0}, \tag{16}$$

determine the respective importance of inertia, gravity and surface tension compared with viscosity.

The dimensionless equations and boundary conditions are (dropping tildes)

$$\sigma_{xx} = -p + 2\mu\frac{\partial u}{\partial x}, \tag{17}$$

$$\sigma_{rr} = -p + 2\mu\frac{\partial v}{\partial r}, \tag{18}$$

$$\sigma_{\theta\theta} = -p + 2\mu\frac{v}{r}, \tag{19}$$

$$\sigma_{xr} = \mu\left(\frac{\partial u}{\partial r} + \epsilon^2\frac{\partial v}{\partial x}\right), \tag{20}$$

$$\frac{\partial(ru)}{\partial x} + \frac{\partial(rv)}{\partial r} = 0, \tag{21}$$

$$\epsilon^2\frac{\partial(r\sigma_{xx})}{\partial x} + \frac{\partial(r\sigma_{xr})}{\partial r} + \epsilon^2 \mathrm{S}r = \epsilon^2 \mathrm{R}r\left(u\frac{\partial u}{\partial x} + v\frac{\partial u}{\partial r}\right), \tag{22}$$

$$\frac{\partial(r\sigma_{xr})}{\partial x} + \frac{\partial(r\sigma_{rr})}{\partial r} - \sigma_{\theta\theta} = \epsilon^2 \mathrm{R}r\left(u\frac{\partial v}{\partial x} + v\frac{\partial v}{\partial r}\right), \tag{23}$$

$$\left.\begin{aligned} v &= uh'(x) \\ \sigma_{xr} &= \epsilon^2 h'(x)\left(\sigma_{xx} + \mathrm{C}\kappa\right) \\ \sigma_{rr} + \mathrm{C}\kappa &= h'(x)\sigma_{xr} \end{aligned}\right\} \text{ on } r = h(x), \tag{24}$$

$$\kappa = \frac{1}{h(x)\sqrt{1+\epsilon^2 h'(x)^2}} - \frac{\epsilon^2 h''(x)}{\left(1+\epsilon^2 h'(x)^2\right)^{3/2}}, \tag{25}$$

$$v = \frac{\partial u}{\partial r} = 0 \text{ on } r = 0, \tag{26}$$

$$u = 1, \quad v = 0, \quad h = 1 \quad \text{at } x = 0, \tag{27}$$

$$u = \mathrm{D}, \quad v = 0 \quad \text{at } x = 1. \tag{28}$$

2.3 The slender-fiber limit

If the fiber is slender, in the sense that its radius is significantly smaller than its length L, then the complicated two-dimensional free-boundary problem (17–28) may be greatly

simplified. Formally, we take the limit $\epsilon \to 0$ and seek the solutions as asymptotic expansions of the form

$$u \sim u_0 + \epsilon u_1 + \dots$$

(and similarly v, p, h, μ and the stress components). From the data presented in Table 1, we see that $\varepsilon \lesssim 10^{-3}$ so a small ε approximation should be excellent.

At leading order, (22) and (24b) imply that

$$\sigma_{xr0} = 0 \tag{29}$$

and, therefore, from (20),

$$\frac{\partial u_0}{\partial r} = 0 \quad \Rightarrow \quad u_0 = u_0(x). \tag{30}$$

Since the axial velocity is uniform across the fiber, it follows that, to lowest order in ϵ, *plane sections remain plane*.

Next we integrate (21) and use (26) to obtain

$$v_0 = -\frac{r}{2} u_0'(x). \tag{31}$$

Then the kinematic boundary condition (24a) gives

$$\frac{h_0}{2} u_0'(x) + u_0 h_0'(x) = 0 \quad \Rightarrow \quad \frac{d}{dx}\left(u_0 h_0^2\right) = 0$$

and hence, using (27),

$$u_0 h_0^2 = 1, \tag{32}$$

which implies that the flux of liquid along the fiber is uniform.

Next, (23) leads to

$$\frac{\partial p_0}{\partial r} = -\frac{\partial \mu_0}{\partial r} u_0'(x),$$

which may be integrated, applying (24c) to find the leading-order pressure:

$$p_0 = \frac{\mathrm{C}}{h_0} - \mu_0 u_0'(x). \tag{33}$$

We can therefore find all the leading-order stresses,

$$\sigma_{xx0} = -\frac{\mathrm{C}}{h_0} + 3\mu_0 u_0'(x), \quad \sigma_{rr0} = \sigma_{\theta\theta 0} = -\frac{\mathrm{C}}{h_0}, \tag{34}$$

but we are unable to obtain to solve for u_0 and h_0 using the leading-order equations alone.

It is therefore necessary to proceed to $O(\epsilon^2)$, where (22) gives us

$$\sigma_{xr1} = \left\{ \mathrm{R} u_0 u_0' - \mathrm{S} - \mathrm{C} \frac{h_0'}{h_0^2} \right\} \frac{r}{2} - \frac{3}{r} \int_0^r \frac{\partial}{\partial x} \left(\mu_0 u_0' \right) r \, dr. \tag{35}$$

Now, by applying (24b) at order ϵ^2, we obtain a second relation between u_0 and h_0, representing a global stress balance in the x-direction:

$$\frac{d}{dx} \left(3 \bar{\mu}_0 h_0^2 u_0' \right) = \mathrm{R} h_0^2 u_0 u_0' - \mathrm{S} h_0^2 - \mathrm{C} h_0', \tag{36}$$

where $\bar{\mu}_0$ is the cross-sectionally averaged leading-order viscosity:

$$\bar{\mu}_0 = \frac{2}{h_0^2} \int_0^{h_0} \mu_0 r \, dr. \tag{37}$$

If $\bar{\mu}_0$ is a known function of x, then (32, 36) is a closed system for $u_0(x)$ and $h_0(x)$, subject to the boundary conditions

$$u_0(0) = 1, \quad h_0(0) = 1, \quad u_0(1) = \mathrm{D}. \tag{38}$$

2.4 Simple example — importance of the draw ratio

The simplest possible scenario is that of a fiber with constant viscosity, for which inertia, gravity and surface tension are all negligible. This case is obtained by setting

$$\mathrm{R} = \mathrm{S} = \mathrm{C} = 0, \quad \mu \equiv 1,$$

so that (36) reduces to

$$\left(3 h_0^2 u_0' \right)' = 0, \tag{39}$$

which is readily solved with (32, 38) to give

$$u_0 = e^{x \ln \mathrm{D}}, \quad h_0 = e^{-x \ln \mathrm{D}/2}. \tag{40}$$

This has an interesting implication. Recall that the quasi-one-dimensional approximation that led to (40) was obtained by taking the limit $\epsilon \to 0$. This amounts to an assumption that the free surface of the fiber has small slope: $dh/dx \ll 1$ (in dimensional variables). The condition $\epsilon \ll 1$ arises from the estimate that h varies by an amount of order H_0 over a distance of order L; however, (40) implies that this actually occurs

over a distance of order $L/\ln \mathrm{D}$. It follows that the asymptotic expansions carried out in §2.3 actually require that

$$\frac{H_0}{L}\ln \mathrm{D} \ll 1.$$

For the data in Table 1, this inequality is still satisfied, though less clearly at large draw ratios ($H_0 L/(\ln \mathrm{D}) \sim 10^{-2}$–$10^{-1}$).

In practice, this probably means that there may be a small two-dimensional region near the top of the fiber where the theory of §2.3 fails, although it should be fine once the fiber thins further downstream.

2.5 Do plane sections remain plane?

As previously pointed out, the fact that u_0 is independent of r means that, to lowest order, plane sections do remain plane. However, since

$$\frac{\partial u_1}{\partial r} = \frac{r}{2}u_0'' + \frac{\sigma_{xr1}}{\mu_0}, \tag{41}$$

we see that u_1 does, in general, depend on r. Equation (35) implies that radial variations in u_1 may be caused by inertia, gravity or surface tension, or by having a nonuniform viscosity. None of these is necessary, however, as we now illustrate by considering the same simple regime as in §2.4.

In this case, (41) gives

$$\frac{\partial u_1}{\partial r} = -ru_0''$$

and, without loss of generality, by absorbing an appropriate function of x into u_0, we may write

$$u_1 = u_0''\left(\frac{h_0^2}{4} - \frac{r^2}{2}\right) = \ln^2 \mathrm{D}\left(\frac{1}{4} - \frac{r^2}{2}e^{x\ln \mathrm{D}}\right) \tag{42}$$

(using (40)). Hence we find that u_1 is nonuniform across the fiber even for a viscous-dominated Newtonian liquid.

We can use (21) to obtain

$$v_1 = \ln^3 \mathrm{D}\frac{r^3}{8}e^{x\ln \mathrm{D}}, \tag{43}$$

and thus the velocity field in this simple case takes the form

$$u \sim e^{x\ln \mathrm{D}} + \epsilon^2 \ln^2 \mathrm{D}\left(\frac{1}{4} - \frac{r^2}{2}e^{x\ln \mathrm{D}}\right), \tag{44}$$

$$v \sim -\ln \mathrm{D}\frac{r}{2}e^{x\ln \mathrm{D}} + \epsilon^2 \ln^3 \mathrm{D}\frac{r^3}{8}e^{x\ln \mathrm{D}}. \tag{45}$$

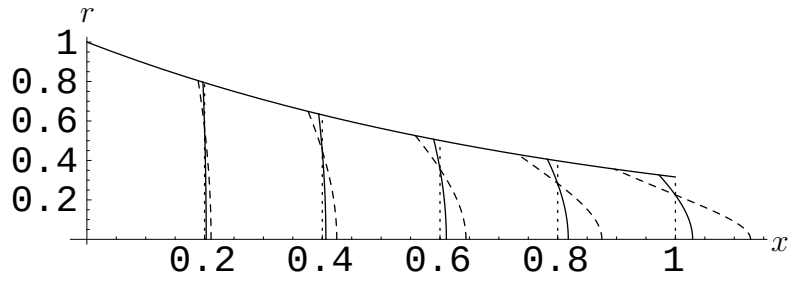

Figure 2: A slender Newtonian fiber with draw ratio D = 10. The shapes of material sections that started uniform at $x = 0$ are shown for $\epsilon = 0$ (dotted lines), $\epsilon = 0.1$ (solid lines), $\epsilon = 0.2$ (dashed lines).

This provides further illustration of the importance of the parameter $\epsilon \ln \mathrm{D}$ — the expansions appear to be uniform only when

$$\varepsilon \ln D \ll 1,$$

which is generally satisfied by the data in Table 1. We can obtain the evolving shape of an initially plane section by solving

$$\frac{dx}{dt} = u(x,r), \quad \frac{dr}{dt} = v(x,r), \quad x(0) = 0, \quad r(0) = s,$$

with (u, v) given by (44, 45). The solution is

$$x = \frac{1}{m} \ln \left\{ \frac{\epsilon^2 m^2 e^T}{[1 + (e^T - 1)s^2]\,[\epsilon^2 m^2 - (e^T - 1)(4 - \epsilon^2 m^2 s^2)]} \right\} \tag{46}$$

$$r = \frac{s}{\epsilon m} \sqrt{\epsilon^2 m^2 - (e^T - 1)(4 - \epsilon^2 m^2 s^2)}, \tag{47}$$

where m and T are used as shorthand for $\ln \mathrm{D}$ and $\epsilon^2 m^3 t/4$. Then a streakline, representing a material section that started at $x = 0$, is obtained by fixing t and plotting (x, r) for s between 0 and 1. We show typical plots in figure 2 for a fiber with D = 10. If we set $\epsilon = 0$, then the plane sections do remain plane, as illustrated by the dotted lines. When ϵ is increased to 0.1, there is a noticeable deformation of the sections, and this becomes quite dramatic after a further increase to 0.2.

At this point, we have developed a theory for how the shape of the drawn glass fiber should behave as a function of physical parameters, and how the glass within the fiber flows. In particular, the flow of the glass fiber in the neck-down region is described to leading order by the equations (40), while the glass fiber in the tube behaves essentially like a continuously drawn fiber entering from the final bushing plate and moving at constant velocity U_1 with constant radius H_1. In the remainder of the report, we consider

the structure of the air flow near the fiber, which is important in understanding the transfer of heat from the fiber to the atmosphere. We examine the structure of the boundary layer air flow in the neckdown region in §3, and in the tube in §4.

3 The boundary layer on the fiber in the neck-down region

As shown in §2.4, a slender Newtonian fiber that flows from a nozzle (which we take to be at position $x = 0$) with velocity U_0 and radius H_0, and is drawn at speed U_1 through a final bushing plate with aperture radius H_1 located at $x = L$ has radius $h(x)$ and surface velocity $U(x)$ given approximately by

$$h(x) = H_0 \mathrm{D}^{-x/2L}, \quad U(x) = U_0 \mathrm{D}^{x/L}, \tag{48}$$

where $\mathrm{D} = U_0/U_1$ is the draw ratio. Conservation of mass of the glass, along with the incompressibility and near-uniformity of the velocity through a cross section, requires that $U_1 H_1^2 = U_0 H_0^2$. This determines U_0 in terms of the other parameters which can be set by design. It will be useful in what follows to identify the length scale

$$\ell = L/\ln D$$

over which the glass fiber properties vary. The typical values for this and some of the other derived parameter values are summarized in Table 2.

Table 2: Approximate values of some derived physical parameters [2, 8, 11]. Primitive physical parameters listed in Table 1.

Draw ratio	$\mathrm{D} \approx 10^4$–10^6 ,
Fiber length scale	$\ell \approx 5$–10 cm,
Initial fiber velocity	$U_0 \approx 0.1$–100 mm/s,
Initial air Reynolds number	$\mathrm{Re}_{a0} \approx 1$–$1000$,
Final air Reynolds number	$\mathrm{Re}_{a1} \approx 10^5$–$10^6$,
Ratio of fiber radius to boundary layer thickness	$a \approx 10^{-2}$–10^{-1}

We begin in §3.1 with some crude preliminary estimates for how the thickness of the boundary layer should behave, and then use these estimates to motivate a more detailed analysis of the boundary layer structure in §3.2.

3.1 Integral Method Estimate for Boundary Layer Thickness

To help organize a mathematical analysis of the boundary layer in the neck-down region, it is useful to get some idea of how thick the boundary layer should be. That is, we seek to estimate to what distance about the fiber the air is noticably accelerated due to momentum transfer from the moving glass fiber.

First, we estimate the Reynolds number of the air flow near the fiber. Since the surface velocity of the fiber varies strongly in the neck-down region, we should consider the Reynolds number *of the air motion* as a function of the distance along the fiber $\mathrm{Re}_a = \mathrm{Re}_a(x)$. (This Reynolds number is to be distinguished from the one defined in (16), referring to the glass flow itself). The local velocity scale is clearly $U(x)$, and the appropriate length scale along the boundary is ℓ. Therefore:

$$\mathrm{Re}_a(x) = \frac{U(x)\ell}{\nu_a} = \frac{U_0\ell}{\nu_a}\mathrm{D}^{x/L}.$$

Using the data from Table 1, we obtain estimates for the Reynolds number near the initial nozzle $\mathrm{Re}_{a0} \equiv \mathrm{Re}_a(0) \sim$ 1–1000 and near the final bushing plate $\mathrm{Re}_{a1} \equiv \mathrm{Re}_a(L) \sim 10^5$–$10^6$. We see therefore in most situations, the Reynolds number is large over most of the fiber, except possibly at the very beginning where the flow can be very slow. Consequently, we expect to be able to use boundary layer theory from fluid mechanics [4], which exploits the fact that at high Reynolds number the air flow varies on a much smaller length scale in the direction normal to the boundary than it does along the boundary.

To this end, we begin with the following approximate expression which is the basis of many "integral method" analyses commonly used by engineers in computing the properties of boundary layers [3, 9, 11]:

$$\frac{d}{dx}\left(\int_{h(x)}^{\infty} u^2(x,r)2\pi r\,dr\right) = -2\pi h(x)\nu_a \left.\frac{du}{dr}\right|_{r=h(x)}, \tag{49}$$

where $\nu_a = 0.15\mathrm{cm}^2/\mathrm{s}$ is the kinematic viscosity of air. This equation is simply an integrated form of the equation for momentum transfer along the streamwise (x) direction, where viscous flux along this direction is neglected (since the streamwise gradients should not be large). Also, there is no pressure gradient included because none is imposed on the air flow in the neck-down region. We seek from the integrated momentum equation (49) to estimate the thickness $\delta(x)$ of the boundary layer as a function of distance along the fiber. One can make a precise definition for $\delta(x)$ in terms of radial integrals of the velocity field [7, Sec. VI.4], but we shall only use it as an order of magnitude length scale. By assuming that $u(x,r)$ is characterized by an amplitude $U(x)$ and only the two length scales $\delta(x)$ and $h(x)$, we obtain the following balance, which is only intended to

indicate orders of magnitude (i. e., scaling with respect to the physical parameters):

$$\frac{d}{dx}\left(U^2(x)\delta(x)(\delta(x)+h(x))\right) \sim \nu_a h(x)\frac{U(x)}{\min(\delta(x),h(x))}.$$

Solving this differential equation through an appropriate integrating factor, we obtain:

$$\delta(x) \sim \begin{cases} \frac{\sqrt{\nu_a \int_0^x U^3(x')h^2(x')\,dx'}}{U^2(x)h(x)} & \text{if } \delta(x) \lesssim h(x), \\ \frac{\sqrt{\nu_a \int_0^x U(x')\,dx}}{U(x)} & \text{if } \delta(x) \gtrsim h(x). \end{cases}$$

Substituting in the particular exponential profiles for $U(x)$ and $h(x)$ from (48), we find:

$$\delta(x) \sim \sqrt{\frac{\nu_a \ell}{U(x)}}.$$

In particular, the ratio of the boundary layer thickness to the length scale of variation of the fiber is:

$$\frac{\delta(x)}{\ell} \sim \sqrt{\frac{\nu_a}{U(x)\ell}} = (\mathrm{Re}_a(x))^{-1/2},$$

which from our estimates for the Reynolds number (Table 2) should be small for most of the fiber, except possibly near the initial nozzle. Also,

$$\frac{h(x)}{\delta(x)} \sim \sqrt{\frac{U_1 H_1^2}{\nu_a \ell}}, \tag{50}$$

which from the data in Table 1, is on the order of 10^{-2}–10^{-1}.

All told then, away from the initial nozzle, we expect the boundary layer of air motion to be very thin compared to the length scale ℓ of variation of the fiber, and to be considerably larger than the thickness of the fiber. The ratio between the boundary layer thickness and the fiber thickness, however, is predicted to remain relatively constant over the whole neckdown region. This means in particular that the boundary layer will, after its intial development, become thinner as it proceeds along the fiber. This may seem counterintuitive, but is quite plausible. The rapid stretching of the fiber accelerates the air rapidly downstream, and this streamwise acceleration entrains surrounding air closer to the fiber due to incompressibility of the air flow. This radial entrainment compresses the boundary layer closer to the fiber.

We prepare now to develop a more detailed theory to describe the structure of the boundary layer motion of the air. To do this, we will use the proper boundary layer equations which result from the observation that the boundary layer is slender

($\delta(x) \ll \ell$) at least away from the initial nozzle. We will treat the ratio between the fiber radius $h(x)$ and the boundary layer thickness $\delta(x)$ as an $O(1)$ quantity, though the data presented in Table 2 suggests that we might treat $h(x)/\delta(x)$ as a small quantity in an asymptotic treatment. This would amount to modeling the fiber as an infinitely thin line source, which creates a number of subtleties in the asymptotic analysis [5, 6, 12]. We opt therefore to retain a finite thickness for the fiber in our mathematical equations, but note that the results remain uniformly valid even if the fiber thickness becomes very small.

3.2 Detailed Structure of Boundary Layer near Fiber

We seek now to find the air flow in the boundary layer surrounding the fiber. We use cylindrical polar coordinates (x, r), and denote the components of the velocity field of the air motion by (u, v) in the same coordinate system. Note that we are using the same symbols for the air velocity here as we did for the glass velocity in §2, but since we will no longer refer to the internal glass motion, we indulge in this convenient recycling of notation. Motivated by the crude estimate for the boundary layer thickness developed in §3.1, we nondimensionalise variables as follows:

$$x = \ell\tilde{x}, \quad r = \sqrt{\frac{\nu_a \ell}{U_0}}\tilde{r}, \quad u = U_0\tilde{u}, \quad v = \sqrt{\frac{\nu_a U_0}{\ell}}\tilde{v},$$

Since we have argued that the boundary layer should be thin compared to the streamwise length scale of variation of the fiber ℓ, we can work with Prandtl's boundary layer equations rather than the full Navier-Stokes equations. In our cylindrical geometry (with no imposed pressure gradient), these equations read (dropping tildes)

$$u_x + \frac{1}{r}(rv)_r = 0 \tag{51}$$

$$(uu_x + vu_r) = u_{rr} + \frac{u_r}{r}, \tag{52}$$

The corresponding boundary conditions are

$$u = e^x, \quad v = -a\frac{e^{x/2}}{2} \quad \text{on} \quad r = ae^{-x/2}, \tag{53}$$

$$u \to 0 \quad \text{as} \quad r \to \infty. \tag{54}$$

where

$$a \equiv \sqrt{\frac{U_0 H_0^2}{\nu_a \ell}} = \sqrt{\frac{U_1 H_1^2}{\nu_a \ell}}$$

is the ratio between the fiber thickness and boundary layer thickness (compare with (50)).

The boundary layer equations (51–53) are a little different than the standard boundary layer equations because the fiber has width comparable (or smaller than) the thickness of the boundary layer. The standard theory typically assumes the boundary layer is thin compared to all length scales characterizing the fluid boundary, in which case the "flat-plate" equations are appropriate in certain body-oriented coordinates [4]. The thinness of the fiber requires the inclusion of the last term in (52) ([7, Sec. VIII.1],[11]). We remark that boundary layer equations equivalent to (51–53) can be derived by working in a body-oriented coordinate system and carefully keeping the important terms under the assumption that the boundary layer is thin compared to ℓ, but of comparable or larger width than the radius of the fiber. We stress that the boundary layer equations (51–53) are valid for those regions of the fiber where $\mathrm{Re}_a(x) \gg 1$ (so that $\delta(x)/\ell = (\mathrm{Re}_a(x))^{-1/2} \ll 1$), and remain uniformly valid for small or order unity values of a, the ratio of fiber and boundary layer thickness.

It is fortunate that this problem admits a similarity solution of the form

$$u = e^x f(\eta), \quad v = e^{x/2} g(\eta), \quad \eta = r e^{x/2}. \tag{55}$$

Substitution of (55) into (51) leads to

$$\eta f + \frac{\eta^2}{2} f' + g + \eta g' = \left(\frac{\eta^2}{2} f + \eta g \right)' = 0.$$

The bracketed term must be a constant which (53) implies is zero and hence

$$g(\eta) = -\frac{\eta}{2} f(\eta). \tag{56}$$

Then (52) gives rise to an ordinary differential equation for $f(\eta)$,

$$f'' + \frac{f'}{\eta} = f^2, \tag{57}$$

with boundary conditions

$$f(a) = 1, \quad f(\infty) = 0. \tag{58}$$

We use the transformation

$$f(\eta) = \frac{4F(t)}{\eta^2}, \quad \eta = a e^t, \tag{59}$$

to turn (57) into the autonomous nonlinear ordinary differential equation

$$\frac{d^2 F}{dt^2} - 4\frac{dF}{dt} + 4F = 4F^2, \tag{60}$$

with boundary conditions

$$F(0) = a^2/4, \quad F(t) = o(e^{2t}) \text{ as } t \to \infty. \tag{61}$$

The solution to this equation can be analyzed through phase plane methods [10] by plotting trajectories for (F, G) where $G = \frac{dF}{dt}$. We find an unstable source at $(F, G) = (0, 0)$ and a saddle point at $(F, G) = (1, 0)$, and no other fixed points or limit cycles. Any trajectory must either approach the saddle point $(1, 0)$ along its stable manifold or shoot off to infinity. Some further asymptotic analysis for when F becomes large shows that trajectories which grow infinitely large do so in finite time. Consequently, the solution to (60–61) must have $\lim_{t\to\infty}(F(t), G(t)) = (1, 0)$ in order to satisfy the $t \to \infty$ boundary condition in (61). Local analysis near this saddle point shows moreover that

$$F(t) \sim 1 \pm e^{2(1-\sqrt{2})(t+t_0)} \text{ as } t \to \infty,$$

where the arbitrary translation t_0 must be chosen to make $F(a) = 1$ and the $\pm$ is equal to the sign of $(a^2 - 4)$. In fact, all solutions of (60, 61) can be written in terms of two canonical solutions satisfying

$$\frac{d^2\Phi_\pm}{d\tau^2} - 4\frac{d\Phi_\pm}{d\tau} + 4\Phi_\pm - 4\Phi_\pm^2 = 0, \tag{62}$$

$$\Phi_\pm \sim 1 \pm e^{2(1-\sqrt{2})\tau} \text{ as } \tau \to \infty. \tag{63}$$

These canonical solutions are simply a description of the trajectories which form the two branches of the stable manifold of the saddle point $(F, G) = (1, 0)$. The solution $F(t)$ to (60–61) is given by

$$F(t) = \begin{cases} \Phi_+(t + t_0) & \text{if } a > 2, \\ \Phi_-(t + t_0) & \text{if } a < 2, \end{cases}$$

where the translation t_0 is chosen so that $F(0) = a^2/4$. The canonical solution Φ_- seems most appropriate for the glass fiber drawing application, since $a \lesssim 10^{-1}$. Numerical solutions for $\Phi_\pm$ are plotted in figure 3. We see that both are monotonic;

$$\Phi_- \sim \tau e^{2\tau} \text{ as } \tau \to -\infty,$$

while Φ_+ blows up at a finite value of τ:

$$\Phi_+ \sim \frac{3}{2}\left(\tau - \tau^*\right)^{-2},$$

where $\tau^* \approx -0.85$.

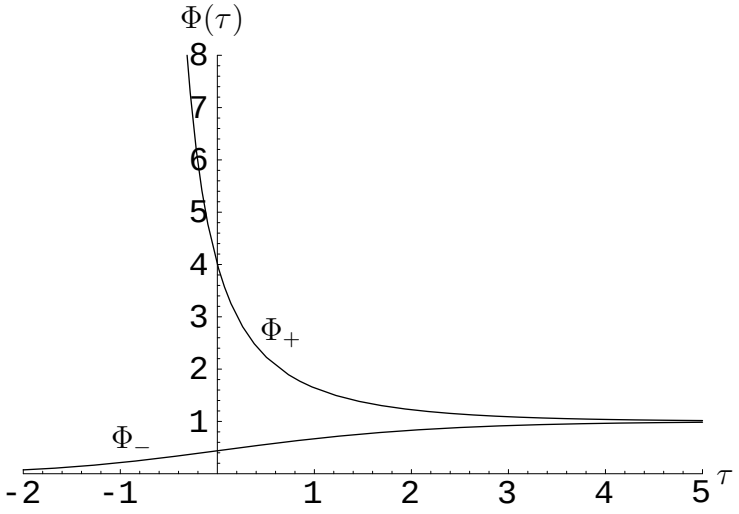

Figure 3: The functions $\Phi_{\pm}(\tau)$ satisfying (62, 63).

Once F has been determined by the procedure outlined above, the velocity field is given by

$$u = \frac{4F\left(\frac{x}{2} + \ln\left(\frac{r}{a}\right)\right)}{r^2}, \quad v = -\frac{2F\left(\frac{x}{2} + \ln\left(\frac{r}{a}\right)\right)}{r}. \tag{64}$$

We plot the flow field for three different values of a in figure 4. The middle plot is the special case $a = 2$ for which $F \equiv 1$ and the flow is actually independent of x. There is not a huge qualitative difference between the upper and lower plots, for which $a = 1$ and $a = \sqrt{20}$ respectively (so the former uses Φ_- and the latter Φ_+). It is noticeable, however, that the ratio of the boundary layer to the fiber grows thinner as a increases, as it should.

3.2.1 Search for general similarity solutions for boundary layer of stretched fiber

In addition to solving for the boundary layer structure according to the particular fiber shape laws (48) which arise for the present application, we considered as well the basic question of what types of fiber shapes and surface velocity profiles admit similarity solutions. This inquiry is motivated by the great usefulness which similarity solutions have enjoyed in various boundary layer analyses. Their mathematical utility is in the reduction of a two-dimensional partial differential equation to a one-dimensional ordinary differential equation which can be analyzed and numerically solved much more easily. Since there does not seem to be much work on studying the boundary layers near stretching fibers, we sought to find more general situations where the method of similarity solutions may permit a quick analysis of the boundary layer structure.

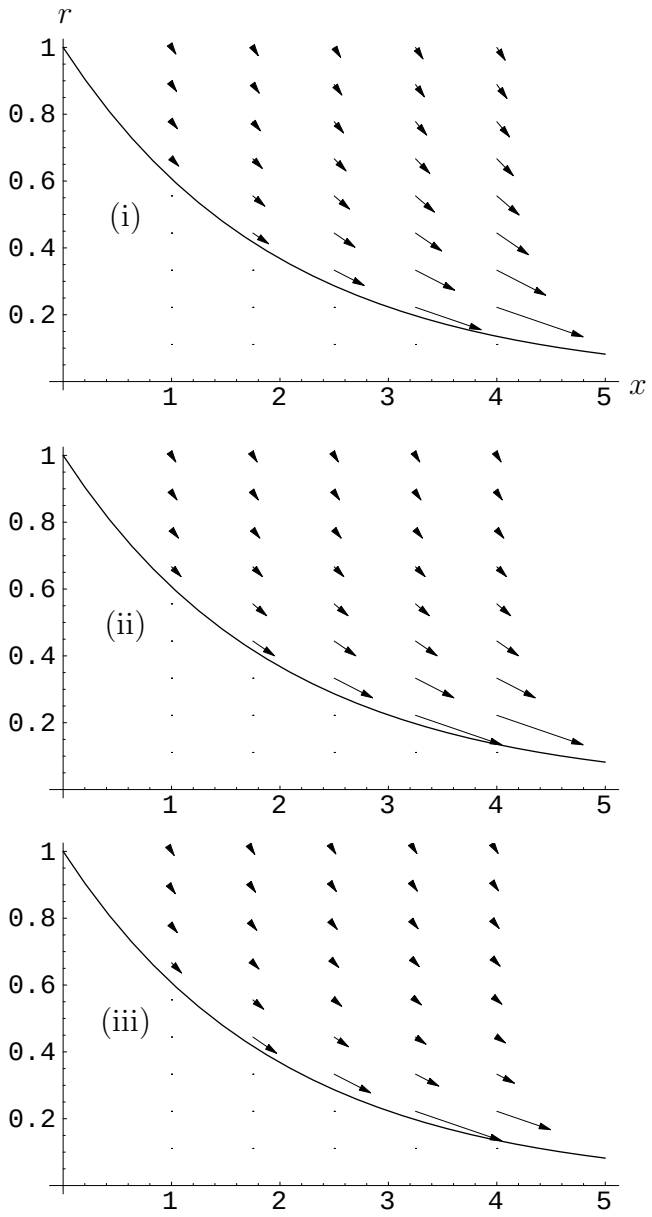

Figure 4: The flow field in the boundary layer past the fiber $r = e^{-x/2}$; (i) $a = 1$, (ii) $a = 4$, (iii) $a = \sqrt{20}$.

Therefore, we consider the nondimensional system

$$[uu_x + vu_r] = u_{rr} + \frac{1}{r}u_r, \tag{65}$$

$$u_x + \frac{1}{r}(rv)_r = 0, \tag{66}$$

subject to the nondimensional boundary conditions

$$r = \tilde{h}(x): \quad u = \tilde{U}(x), \quad v = \tilde{h}'(x)\tilde{U}(x), \tag{67}$$

$$r \to \infty: \quad u \to 0, \quad v \to 0. \tag{68}$$

We do not here assume a particular functional form for $\tilde{U}(x)$ and $\tilde{h}(x)$, but rather wish to determine what types of velocity profiles $\tilde{U}(x)$ on the fiber boundary and what fiber shapes $\tilde{h}(x)$ permit nontrivial similarity solutions to (65)-(68). (Since these functions are specified inputs, we put tildes on them to stress that these are to be represented as nondimensionalized functions).

We introduce the transformations

$$u = s(x)z(\xi), \quad v = q(x)w(\xi), \tag{69}$$

where z and w are functions of the similarity variable

$$\xi = \frac{r}{g(x)}. \tag{70}$$

Substitution of (69) into the equations (65)-(66) yields

$$s\left(\left[s'z^2 - \frac{g's}{g}\xi z\frac{dz}{d\xi} + \frac{q}{g}w\frac{dz}{d\xi}\right] - \frac{1}{g^2}\left[\frac{d^2z}{d\xi^2} + \frac{1}{\xi}\frac{dz}{d\xi}\right]\right) = 0, \tag{71}$$

$$s'z - \frac{g's}{g}\xi\frac{dz}{d\xi} + \frac{q}{g}\left[\frac{dw}{d\xi} + \frac{1}{\xi}w\right] = 0, \tag{72}$$

where

$$s \equiv s(x), \quad q \equiv q(x), \quad g \equiv g(x),$$

and the prime ($'$) designates differentiation with respect to x. In order for the equations (71)-(72) and the similarity variable (70) to be nonsingular, the function $g(x)$ must be nonzero. Furthermore, nontrivial similarity solutions do not exist when $s(x)$ or $q(x)$ vanish, as is easily checked. Upon substituting (69) into the boundary conditions (67), we write

$$\xi = \frac{\tilde{h}(x)}{g(x)}: \quad z = \frac{\tilde{U}(x)}{s(x)}, \quad w = \frac{\tilde{h}'(x)\tilde{U}(x)}{q(x)}, \tag{73}$$

$$\xi \to \infty : \quad z \to 0, \quad w \to 0. \tag{74}$$

The new dependent variables, z and w, are functions of ξ only. For similarity solutions to exist the system for z and w, (71)-(74), must be independent of x. Elimination of the x-dependence in the boundary conditions (73) necessitates

$$g(x) \propto \tilde{h}(x), \quad s(x) \propto \tilde{U}(x), \quad q(x) \propto h'(x)\tilde{U}(x). \tag{75}$$

For finite z at the boundary we must have $s(x) \not\equiv 0$ (c.f. (73)). Thus, we cancel $s(x)$ in equation (71).

In our analysis of the resulting equation and equation (72), we consider first the case in which $s'(x) = 0$, or $s(x)$ is a constant. In this case the relations (75) reveal that $\tilde{U}(x)$ is a constant, $q(x) \propto \tilde{h}'(x)$, and $g(x) \propto \tilde{h}(x)$. Elimination of the x-dependence in the equations (71)-(72) is possible when

$$\tilde{U}(x) \propto 1, \quad g(x) \propto \sqrt{x}, \quad \tilde{h}(x) \propto \sqrt{x}, \quad q(x) \propto 1/\sqrt{x}. \tag{76}$$

Thus, a constant velocity profile $\tilde{U}(x)$ and a fiber shape $\tilde{h}(x) \propto \sqrt{x}$, permit similarity solutions to (65)-(68).

We now consider the case in which $s'(x) \neq 0$. Dividing (71) through by $s(x)s'(x)$, and dividing (72) through by $s'(x)$ leads to

$$\left[z^2 - a_1\xi z\frac{dz}{d\xi} + a_2 w\frac{dz}{d\xi}\right] - a_3\left[\frac{d^2z}{d\xi^2} + \frac{1}{\xi}\frac{dz}{d\xi}\right] = 0, \tag{77}$$

$$z - a_1\xi\frac{dz}{d\xi} + a_2\left[\frac{dw}{d\xi} + \frac{1}{\xi}w\right] = 0, \tag{78}$$

where

$$a_1 = \frac{g'(x)s(x)}{g(x)s'(x)}, \quad a_2 = \frac{q(x)}{g(x)s'(x)}, \quad a_3 = \frac{1}{g^2(x)s'(x)}. \tag{79}$$

For similarity solutions to exist each of the coefficients a_1, a_2, and a_3 must be constant or must be multiplied by a term that equals zero. The latter possibilities (i.e., when one or more of the terms multiplying a_1, a_2, or a_3 vanish) yield no similarity solutions, as can be checked. Next, we consider the former possibility in which the coefficients a_1, a_2, and a_3 are all constants. This fact, along with the information in (75), leads to the two conditions

$$\frac{\tilde{h}'(x)}{\tilde{h}(x)} \propto \frac{\tilde{U}'(x)}{\tilde{U}(x)}, \qquad \tilde{h}^2(x) \propto \frac{1}{\tilde{U}'(x)}. \tag{80}$$

The latter condition reveals that $\tilde{h}(x) \propto [\tilde{U}'(x)]^{-1/2}$, and hence $\tilde{h}'(x) \propto \tilde{U}''[\tilde{U}'(x)]^{3/2}$. Use of these relations in the first condition in (80) leads to the ordinary differential equation

$$\tilde{U}\tilde{U}'' - c_1 \left(\tilde{U}'\right)^2 = 0, \tag{81}$$

where $\tilde{U}' \equiv d\tilde{U}/dx$, and c_1 is an arbitrary constant. This nonlinear equation can be separated and integrated as

$$\int \frac{\tilde{U}''(x)}{\tilde{U}'(x)} \ dx = c_1 \int \frac{\tilde{U}'(x)}{\tilde{U}(x)} \ dx. \tag{82}$$

Performing the integration we obtain

$$\ln|\tilde{U}'(x)| = c_1 \ln|\tilde{U}(x)| + C, \tag{83}$$

where C is an arbitrary constant. Equation (83) admits general solutions of the form

$$c_1 \neq 1: \qquad \tilde{U}(x) \propto (A_1 + A_2 x)^{\beta}, \quad \beta \equiv 1/(1-c_1), \tag{84}$$

$$c_1 = 1: \qquad \tilde{U}(x) \propto e^{A_2 x}, \tag{85}$$

where A_1 and A_2 are arbitrary constants. We recall that the latter condition in (80) determines the corresponding form of $\tilde{h}(x)$ for a given form of $\tilde{U}(x)$. We find that the system (65)-(68) permits similarity solutions for velocity profiles $\tilde{U}(x)$ and fiber shapes $\tilde{h}(x)$ of the form

$$c_1 \neq 1: \qquad \tilde{U}(x) \propto (A_1 + A_2 x)^{\beta}, \quad \tilde{h}(x) \propto (A_1 + A_2 x)^{\frac{1-\beta}{2}}, \tag{86}$$

$$c_1 = 1: \qquad \tilde{U}(x) \propto e^{A_2 x}, \quad \tilde{h}(x) \propto e^{-A_2 x/2}. \tag{87}$$

Overall, we have determined that the following types of velocity profiles and fiber shapes permit similarity solutions to (65)-(68), without enforcing conservation of mass in the fiber flow: nonlinear functions proportional to $\sqrt{x}$ (76), powers of linear functions of x (86), and exponential solutions (87). Note that many of these solutions are only defined on a semi-infinite interval $x \geq x_0$, which is naturally associated to a fiber which starts abruptly at $x = x_0$ and continues indefinitely (or in practial terms, a substantial distance) toward the right.

We now impose the additional constraint of fiber mass conservation. Assuming the velocity profile within the fiber is relatively flat in the radial direction and that the flow of the fiber is incompressible, we should expect the following linkage between the fiber thickness and surface velocity:

$$\tilde{h}^2(x) \propto \frac{1}{\tilde{U}(x)}. \tag{88}$$

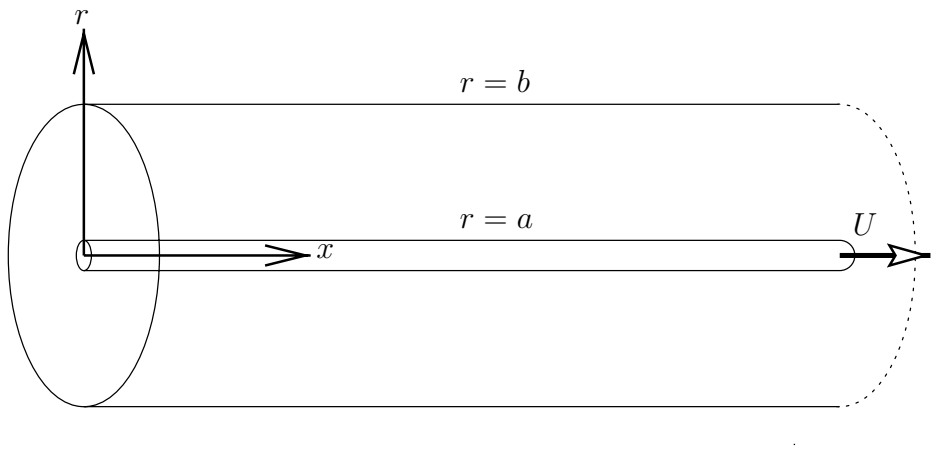

Figure 5: Schematic drawing of a fiber being drawn through a cylinder.

The aforementioned class (76) consisting of the velocity $\tilde{U}(x) \propto 1$ and the shape $\tilde{h}(x) \propto \sqrt{x}$, which pertains to the case $s'(x) \equiv 0$, does not conserve fiber mass.

The case $s'(x) \neq 0$ is more interesting. Fiber mass conservation, coupled with the latter relation in (80), leads us to the condition $\tilde{U}(x) \propto \tilde{U}'(x)$. Hence, $\tilde{h}(x) \propto \tilde{h}'(x)$ by the first relation in (80). These facts reveal that, when fiber mass conservation is enforced, only exponential forms of $\tilde{h}(x)$ and $\tilde{U}(x)$ permit similarity solutions to (65)-(68), i. e.,

$$\tilde{h}^2(x) \propto \frac{1}{\tilde{U}(x)} : \quad \tilde{U}(x) \propto e^{A_2 x}, \quad \tilde{h}(x) \propto e^{-A_2 x/2}, \tag{89}$$

where A_2 is an arbitrary constant. Happily, this is precisely the case in which we are most interested!

4 The boundary layer on the fiber in the cylindrical tube

4.1 Governing equations and nondimensionalisation

In this section we analyse the air flow past the fiber in the tube depicted in Figure 1. To do this, we consider the model problem illustrated in figure 5, using cylindrical polar coordinates (x, r). A cylinder of radius b is closed at $x = 0$. A fiber of radius a is pulled at speed U along the axis of the cylinder through a hole cut in the plane $x = 0$. We wish to determine the flow (u, v) in the air surrounding the fiber.

We assume that the flow is adequately modelled everywhere by the boundary-layer

equations,

$$\frac{\partial(ru)}{\partial x} + \frac{\partial(rv)}{\partial r} = 0, \tag{90}$$

$$u\frac{\partial u}{\partial x} + v\frac{\partial u}{\partial r} = -\frac{1}{\rho}\frac{dp}{dx} + \frac{\nu}{r}\frac{\partial}{\partial r}\left(r\frac{\partial u}{\partial r}\right), \tag{91}$$

where ρ and ν are the density and kinematic viscosity of the air and $p(x)$ is the pressure. The boundary conditions are

$$u = 0 \quad \text{on} \quad x = 0, \quad a < r < b, \tag{92}$$

$$u = v = 0 \quad \text{on} \quad r = b, \quad x > 0, \tag{93}$$

$$u = U, \quad v = 0 \quad \text{on} \quad r = a, \quad x > 0; \tag{94}$$

in the boundary-layer approximation we do not expect to have to impose any downstream conditions.

We nondimensionalise as follows:

$$x = L\tilde{x}, \quad r = b\tilde{r}, \quad u = U\tilde{u}, \quad v = \frac{bU}{L}\tilde{v}, \quad p = \rho U^2\tilde{p},$$

where

$$L = \frac{Ub^2}{\nu} \tag{95}$$

is the length scale over which we expect the boundary to develop until it fills the tube. The resulting dimensionless equations and boundary conditions are (dropping tildes)

$$\frac{\partial(ru)}{\partial x} + \frac{\partial(rv)}{\partial r} = 0, \tag{96}$$

$$u\frac{\partial u}{\partial x} + v\frac{\partial u}{\partial r} = -\frac{dp}{dx} + \frac{1}{r}\frac{\partial}{\partial r}\left(r\frac{\partial u}{\partial r}\right), \tag{97}$$

$$u = 0 \quad \text{on} \quad x = 0, \quad \epsilon < r < 1, \tag{98}$$

$$u = v = 0 \quad \text{on} \quad r = 1, \quad x > 0, \tag{99}$$

$$u = 1, \quad v = 0 \quad \text{on} \quad r = \epsilon, \quad x > 0, \tag{100}$$

where

$$\epsilon = \frac{a}{b}. \tag{101}$$

The radius of the fiber is typically very much smaller than that of the cylinder, so we will analyse the problem asymptotically in the limit $\epsilon \to 0$. Before doing so, it is useful

to observe the following exact global mass conservation law. Integation of (96) with respect to r and application of the boundary conditions on $r = \epsilon$ and $r = 1$ shows that the mass flux must be constant and, therefore, equal to zero since it is zero at $x = 0$:

$$\int_\epsilon^1 ur\, dr \equiv 0. \tag{102}$$

4.2 The entry region

As the fiber first emerges from the hole, the boundary layer thickness is initially comparable to the fiber radius. In this entry region, the boundary layer doesn't notice the outer wall: it just sees a quiescent fluid at infinity. We examine this region via the rescaling

$$r = \epsilon\rho, \quad x = \epsilon^2\xi, \quad v = \epsilon^{-1}V, \tag{103}$$

after which the leading-order problem becomes

$$\frac{\partial(\rho u)}{\partial\xi} + \frac{\partial(\rho V)}{\partial\rho} = 0, \tag{104}$$

$$u\frac{\partial u}{\partial\xi} + V\frac{\partial u}{\partial\rho} = \frac{1}{\rho}\frac{\partial}{\partial\rho}\left(\rho\frac{\partial u}{\partial\rho}\right), \tag{105}$$

$$u = 0 \quad \text{on} \quad \xi = 0, \quad \rho > 1, \tag{106}$$

$$u = 1, \quad V = 0 \quad \text{on} \quad \rho = 1, \quad \xi > 0, \tag{107}$$

$$u \to 0 \quad \text{as} \quad \rho \to \infty, \quad \xi > 0. \tag{108}$$

It is worth noting that the boundary-layer equations are strictly applicable to this region only if it is slender, *i.e.* if it is long in the x-direction compared to b. This gives rise to the condition

$$\frac{\varepsilon^2 L}{\varepsilon b} = \frac{\epsilon L}{b} = \frac{Ua}{\nu} \gg 1;$$

in other words, the flow must have a high Reynolds number based on the fiber radius.

4.3 The behaviour as $\xi \to 0$

Even closer to the exit hole $\xi = 0$, where the boundary layer is much thinner than the fiber radius, the flow resembles a classical Blasius boundary layer. To examine this, suppose

$$\xi \ll 1, \quad \rho = 1 + y, \quad y \ll 1, \tag{109}$$

so that (104–108) become

$$\frac{\partial u}{\partial \xi} + \frac{\partial V}{\partial y} \sim 0, \tag{110}$$

$$u\frac{\partial u}{\partial \xi} + V\frac{\partial u}{\partial y} \sim \frac{\partial^2 u}{\partial y^2}, \tag{111}$$

$$u = 0 \quad \text{on} \quad \xi = 0, \quad y > 0, \tag{112}$$

$$u = 1, \quad V = 0 \quad \text{on} \quad y = 0, \quad \xi > 0, \tag{113}$$

$$u \to 0 \quad \text{as} \quad y \to \infty, \quad \xi > 0. \tag{114}$$

This system admits a similarity solution of the form

$$u = f'(\eta), \quad V = \frac{1}{2\sqrt{\xi}}\left(\eta f'(\eta) - f(\eta)\right), \quad \eta = \frac{y}{\sqrt{\xi}}. \tag{115}$$

The function f satisfies the o.d.e. problem

$$f''' + \frac{ff''}{2} = 0,$$

$$f(0) = 0, \quad f'(0) = 1, \quad f'(\infty) = 0, \tag{116}$$

which is readily solved numerically: it transpires that $f''(0) \approx -0.44375$, $f(\infty) \approx 0.61613$.

4.4 The behaviour as $\xi \to \infty$

The similarity solution (115) gives the behaviour of the solution of (104–108) as $\xi \to 0$. Next we investigate the corresponding behaviour at large ξ. As ξ increases, the boundary layer grows until it is much larger than the fiber radius. The boundary condition (107) on $\rho = 1$ may then be replaced by a specified singularity in u at $\rho = 0$. The required singular behaviour is obtained by performing an inner analysis for ρ close to 1 and matching with an outer solution where $\rho \gg 1$.

The inner region may be examined by using an artificial small parameter as follows:

$$\xi = \frac{\tilde{\xi}}{\delta^2}, \quad V = \delta^2 \tilde{V}, \tag{117}$$

where $\delta \ll 1$. The equations and boundary conditions to be applied to the inner problem are

$$\frac{\partial(\rho u)}{\partial \tilde{\xi}} + \frac{\partial(\rho \tilde{V})}{\partial \rho} = 0, \tag{118}$$

$$\delta^2\left(u\frac{\partial u}{\partial \tilde{\xi}} + \tilde{V}\frac{\partial u}{\partial \rho}\right) = \frac{1}{\rho}\frac{\partial}{\partial \rho}\left(\rho\frac{\partial u}{\partial \rho}\right), \tag{119}$$

$$u = 1, \quad V = 0 \quad \text{on} \quad \rho = 1, \tag{120}$$

and the leading-order solution is

$$u \sim 1 + A(\tilde{\xi}) \log \rho, \tag{121}$$

$$\tilde{V} \sim -\frac{dA}{d\tilde{\xi}} \frac{1 + 2\rho \log \rho - \rho}{4}, \tag{122}$$

for some (as yet) arbitrary function $A(\tilde{\xi})$.

The outer region is found via the further scaling

$$\rho = \frac{\hat{\rho}}{\delta}, \quad \tilde{V} = \frac{\hat{V}}{\delta} \quad \Rightarrow \quad V = \delta \hat{V}, \tag{123}$$

after which the full boundary-layer equations are recovered,

$$\frac{\partial(\hat{\rho} u)}{\partial \tilde{\xi}} + \frac{\partial(\hat{\rho} \hat{V})}{\partial \hat{\rho}} = 0, \tag{124}$$

$$u \frac{\partial u}{\partial \tilde{\xi}} + \hat{V} \frac{\partial u}{\partial \hat{\rho}} = \frac{1}{\hat{\rho}} \frac{\partial}{\partial \hat{\rho}} \left(\hat{\rho} \frac{\partial u}{\partial \hat{\rho}} \right), \tag{125}$$

with

$$u \to 0 \quad \text{as} \quad \hat{\rho} \to \infty \quad \text{and as} \quad \tilde{\xi} \to 0. \tag{126}$$

The boundary condition on $\rho = 1$ is now replaced by a matching condition, namely

$$u \sim 1 + A(\tilde{\xi}) \left\{ \log \hat{\rho} + \log(1/\delta) \right\}, \quad \text{as} \quad \hat{\rho} \to 0, \tag{127}$$

$$\hat{V} \to 0 \quad \text{as} \quad \hat{\rho} \to 0. \tag{128}$$

This problem resembles some studied previously by Mike Ward and Joe Keller [6, 5, 12]. The idea is that, if the singular part of u is given, *i.e.* if

$$u \sim A(\tilde{\xi}) \log \hat{\rho} + R(\tilde{\xi}) \tag{129}$$

and $A(\tilde{\xi})$ is specified, then the regular remainder $R(\tilde{\xi})$ may be determined by solving (124–126). The problem is then closed by insisting that

$$R(\tilde{\xi}) = 1 + A(\tilde{\xi}) \log(1/\delta). \tag{130}$$

4.5 The fully developed flow

Thus far we have been considering the flow in a neighbourhood of the hole from which the fiber emerges, where the outer cylinder has negligible influence on the boundary layer. Next we examine the other extreme case, namely the fully-developed flow which, presumably, is approached some distance downstream of the hole. If we set $v = 0$, $u = u(r)$ in (96–100), then we find that u takes the form

$$u = -\frac{p'}{4}\left(1 - r^2\right) + \left(1 + \frac{p'}{4}\left(1 - \epsilon^2\right)\right)\frac{\log r}{\log \epsilon}, \tag{131}$$

where the pressure gradient p' is constant. To fix p' we set the net mass flux to zero, as dictated by (102), and hence find

$$p' = -\frac{4}{1-\epsilon^2}\left(\frac{1 + 2\epsilon^2 \log \epsilon - \epsilon^2}{1 - \epsilon^2 + (1+\epsilon^2)\log \epsilon}\right). \tag{132}$$

These expressions may now be simplified by using the fact that ϵ is small. It transpires that the approximation

$$p' \sim \frac{4n}{1-n}, \tag{133}$$

$$u \sim \left(\frac{4n}{1-n}\right)\left(r^2 - 1 - \log r\right) \tag{134}$$

is accurate up to $O(\epsilon^2)$ for all r, where n is used as shorthand for

$$n = \frac{1}{\log(1/\epsilon)}. \tag{135}$$

Some typical velocity profiles are shown in figure 6. The general picture is of a logarithmically singular velocity, due to the traction exerted on the air by the moving fiber, with a weak return flow near the outer wall forced by mass conservation. The approximation (134) is indistinguishable from the exact solution when $\epsilon = 0.01$ and does well for $\epsilon = 0.1$, although the innaccuracy is significant at $\epsilon = 0.2$, especially in the return flow. Notice that the dashed approximate curves all pass through zero at the same value of $r = r_*$, where

$$r_*^2 = 1 + \log r_* \quad \Rightarrow \quad r_* \approx 0.450764. \tag{136}$$

4.6 The developing flow

Thus far we have examined (i) the flow in the entry region where the boundary layer is comparable in thickness to the fiber and (ii) the fully-developed flow that is approached

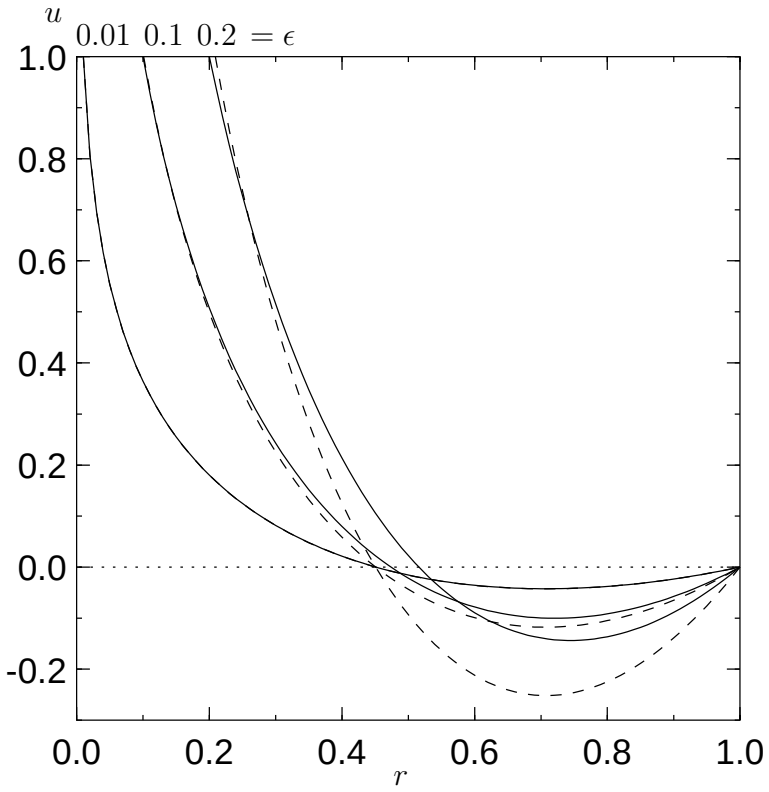

Figure 6: The fully-developed velocity profile for $\epsilon = 0.01,\ 0.1,\ 0.2$. The solid lines show the exact solution (131), the dashed lines the approximation (134).

some distance downstream of the entry hole. It remains to analyse the region between these two, in which the boundary layer develops until it fills the tube. Here the flow is governed by the full boundary-layer equations (96, 97),

$$\frac{\partial(ru)}{\partial x} + \frac{\partial(rv)}{\partial r} = 0, \tag{137}$$

$$u\frac{\partial u}{\partial x} + v\frac{\partial u}{\partial r} = -\frac{dp}{dx} + \frac{1}{r}\frac{\partial}{\partial r}\left(r\frac{\partial u}{\partial r}\right), \tag{138}$$

with boundary conditions

$$u = 0 \quad \text{on} \quad x = 0, \tag{139}$$

$$u = v = 0 \quad \text{on} \quad r = 1, \tag{140}$$

and a matching condition, derived as in §4.4,

$$u \sim A(x)\log r + 1 + \frac{A(x)}{n}, \quad v \to 0 \quad \text{as} \quad r \to 0, \tag{141}$$

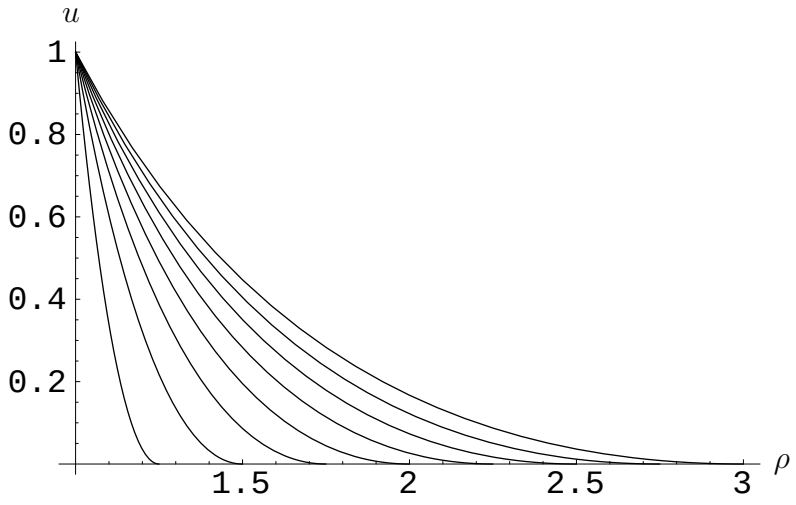

Figure 7: The velocity profile ansatz (143) plotted versus ρ for $\sigma = 1.25$, 1.5, 1.75, 2.0, 2.25, 2.5, 2.75, 3.0.

for some function $A(x)$ (recall that $n = -1/\log\epsilon$).

Since the boundary conditions on $r = \epsilon$ have been shifted to $r = 0$, the flux condition (102) is now approximated by

$$\int_0^1 ur\,dr \equiv 0. \tag{142}$$

Notice that the approximate expression (134) for the fully-developed flow is recovered by seeking a solution of (137, 138, 140, 141, 142) in which $v \equiv 0$ and u is independent of x.

4.7 Integral-balance solution in the entry region

Now we construct an approximate solution to the entry-region equations (104–108) using an *ad hoc* integral-balance method. An analogous approach is applied to the developing boundary-layer flow in §4.8 below. We pose the following ansatz, suggested by the fully-developed flow (131), for the velocity profile:

$$u = \begin{cases} 1 - \dfrac{2\sigma^2\log\rho + 1 - \rho^2}{2\sigma^2\log\sigma + 1 - \sigma^2} & \rho < \sigma(\xi), \\ 0 & r > \sigma(\xi), \end{cases} \tag{143}$$

where $\rho = \sigma(\xi)$ denotes the boundary layer thickness.

As shown in figure 7, this general form satisfies $u = 1$ on $\rho = 1$, while u and $\partial u/\partial r$ are continuous across $r = \sigma$. It also ties in with the "inner-outer" picture found in §4.4 as $\xi \to \infty$. After the rescaling

$$\rho = \frac{\hat{\rho}}{\delta}, \quad \sigma = \frac{\hat{\sigma}}{\delta},$$

the leading-order outer velocity takes the form

$$u \sim 1 - \frac{2\hat{\sigma}^2 \log(\hat{\rho}/\delta) - \hat{\rho}^2}{2\hat{\sigma}^2 \log(\hat{\sigma}/\delta) - \hat{\sigma}^2}.$$

Now taking the limit $\hat{\rho} \to 0$, we have

$$u \sim 1 - \frac{2\log(\hat{\rho}/\delta)}{2\log(\hat{\sigma}/\delta) - 1},$$

which is of the required form

$$u \sim A \log \hat{\rho} + 1 + A \log(1/\delta),$$

where

$$A = \frac{-2}{2\log(\hat{\sigma}/\delta) - 1}.$$

It remains to determine the scalar function $\sigma(\xi)$, which we do by satisfying an integrated form of the momentum equation (105), namely (c. f.(49)

$$\frac{d}{d\xi} \int_1^\sigma u^2 \rho \, d\rho = - \left. \frac{\partial u}{\partial \rho} \right|_{\rho=1}. \tag{144}$$

This reduces to a first-order ordinary differential equation of the form

$$\frac{d}{d\xi} [F(\sigma)] = R(\sigma), \tag{145}$$

where

$$F(\sigma) = \frac{(\sigma^2 - 1)(5\sigma^4 - \sigma^2 + 2) - 12\sigma^2 \log \sigma (1 + 2\sigma^2 \log \sigma)}{12 \left(2\sigma^2 \log \sigma + 1 - \sigma^2\right)^2} \tag{146}$$

$$R(\sigma) = \frac{2(\sigma^2 - 1)}{2\sigma^2 \log \sigma + 1 - \sigma^2}. \tag{147}$$

The solution is therefore

$$\xi = \int_1^\sigma I(\sigma') \, d\sigma', \tag{148}$$

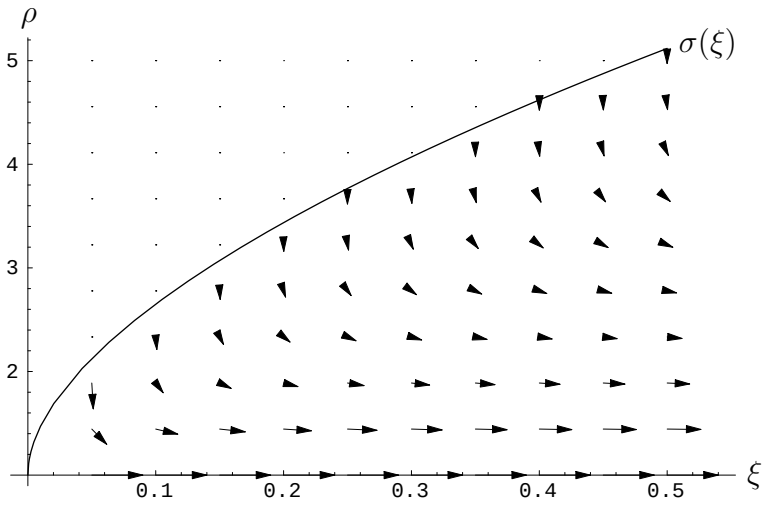

Figure 8: The boundary layer edge $\rho = \sigma(\xi)$ and the flow in the boundary layer.

where $I(\sigma) = \dfrac{F'(\sigma)}{R(\sigma)}$

$$= \frac{\sigma\left\{-3(\sigma^2-1)^2(5\sigma^2+1) + 2\log\sigma(\sigma^2-1)(5\sigma^4+17\sigma^2+2) - 24\sigma^2\log^2\sigma\right\}}{12(\sigma^2-1)\left(2\sigma^2\log\sigma + 1 - \sigma^2\right)^2}. \quad (149)$$

Equation (149) gives the shape of the boundary layer and hence, via (143), the flow field, as shown in figure 8. The asymptotic behaviour may be determined as follows. Near the inlet, σ is close to 1 and

$$I(\sigma) \sim \frac{(\sigma-1)}{10} - \frac{(\sigma-1)^2}{180} + \ldots \quad \Rightarrow \quad \xi \sim \frac{(\sigma-1)^2}{20} - \frac{(\sigma-1)^3}{540} + \ldots,$$

so that

$$\sigma \sim 1 + 2\sqrt{5\xi} + \frac{10\xi}{27} + \ldots \quad \text{as} \quad \xi \to 0. \quad (150)$$

This may be compared with the small-ξ behaviour predicted in §4.3 as follows. With ρ close to 1 and σ given by (150), the velocity profile (143) takes the approximate form

$$u \sim \begin{cases} \left(1 - \dfrac{\eta}{2\sqrt{5}}\right)^2 & \eta < 2\sqrt{5}, \\ 0 & \eta > 2\sqrt{5}, \end{cases} \quad (151)$$

where, as before, $\eta = (\rho - 1)/\sqrt{\xi}$. On the other hand, the similarity solution found in §4.3 has $u = f'(\eta)$ where f satisfies the o.d.e. problem (116). In figure 9 we show that

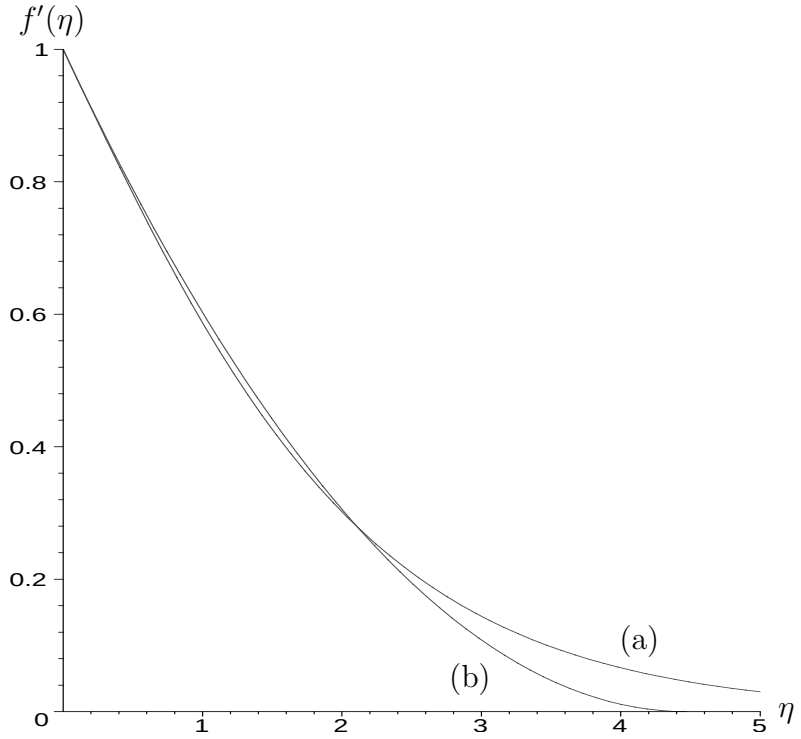

Figure 9: Velocity $u = f'(\eta)$ versus $\eta = y/\sqrt{\xi}$; (a) numerical solution to (116), (b) integral balance solution (151).

the two approximations agree reasonably well. In particular, (151) predicts $f''(0) = -1/\sqrt{5} \approx -0.44721$ which is encouragingly close to the value of -0.44375 found by solving (116) numerically.

The asymptotic behaviour when σ is large is given by

$$I(\sigma) \sim \frac{5\sigma(2\log\sigma - 3)}{12(2\log\sigma - 1)^2} + O\left(\frac{1}{\sigma}\right) \quad \Rightarrow \quad \xi \sim \frac{5\sigma^2}{48\log\sigma}, \tag{152}$$

and hence

$$\sigma \sim 2\sqrt{\frac{6}{5}}\,\sqrt{\xi\log\xi} \quad \text{as} \quad \xi \to \infty.$$

4.8 Integral-balance solution for the developing flow

In the developing flow we propose the following ansatz for the velocity profile that incorporates both the boundary layer near the fiber and the return flow:

$$u = \begin{cases} u_1(s) = 1 + \dfrac{C_1(s)}{n} + C_1(s)\log r + C_2(s)r^2 & 0 < r < s, \\ u_2(s) = C_3(s)\log r + C_4(s)(r^2 - 1) & s < r < 1, \end{cases} \tag{153}$$

chosen to satisfy the no-slip condition (140) on $r = 1$ and the matching condition (141) as $r \to 0$. The four functions $C_i(s)$ are determined from the conditions

$$u(s_+) = u(s_-) = \left[\frac{\partial u}{\partial r}\right]_{s_-}^{s_+} = \int_0^1 ur\,dr = 0,$$

whence

$$u_1 = n\left\{(r^2 - s^2)(1 - s^2) + \left[s^2 - 3s^4 + r^2(1 + s^4)\right]\log s + 2s^2\log s\right.$$

$$\left. -s^2\left[2 - 3s^2 + s^4 + 2\log s\right]\log r\right\}\Big/$$

$$\left\{s^2\left[(1 - s^2)(2 - n - s^2) + (2 + n - 3ns^2)\log s + 2n\log^2 s\right]\right\}, \tag{154}$$

$$u_2 = \frac{ns^2\left\{(1 - s^2)\log r - (1 - r^2)\log s\right\}}{(1 - s^2)(2 - n - s^2) + (2 + n - 3ns^2)\log s + 2n\log^2 s}. \tag{155}$$

The velocity profile ansatz (153) is plotted versus r in figure 10, with $n = 0.1$ and s varying between 0 and 0.45. At small values of s, the velocity is confined to a narrow boundary layer, outside which it is effectively zero. As s increases, the velocity decays less sharply and the return flow becomes more significant. The maximum value of s is r_*, as defined in (136), at which the expressions for u_1 and u_2 are identical and equal to the fully-developed profile (134).

Finally an equation for the boundary-layer thickness $s(x)$ is obtained by applying global conservation of momentum both to the boundary layer and to the return flow. Integration of (138) with respect to r between 0 and s and between s and 1 gives rise to

$$\frac{d}{dx}\int_0^s u_1^2 r\,dr = -\frac{s^2}{2}\frac{dp}{dx} + \left[r\frac{\partial u_1}{\partial r}\right]_0^s, \tag{156}$$

$$\frac{d}{dx}\int_s^1 u_2^2 r\,dr = -\frac{1 - s^2}{2}\frac{dp}{dx} + \left[r\frac{\partial u_2}{\partial r}\right]_s^1, \tag{157}$$

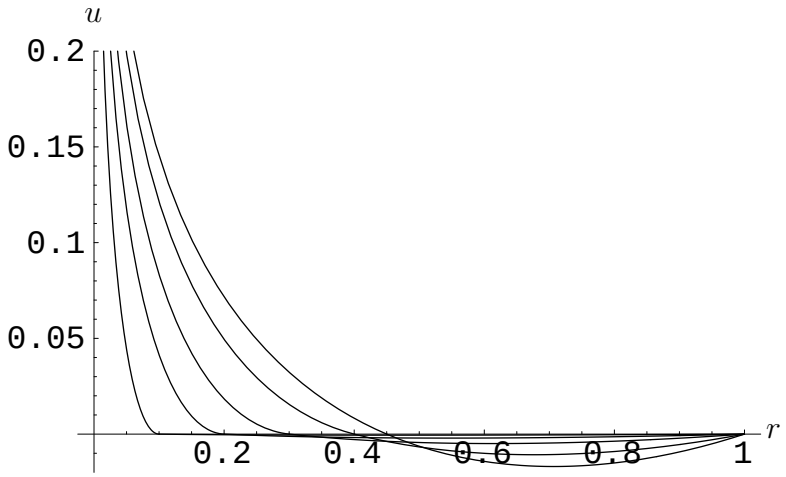

Figure 10: The velocity profile ansatz (153) plotted versus r for $n = 0.1$ and $s = 0.1$, 0.2, 0.3, 0.4, 0.45.

which we write in the form

$$\frac{d}{dx}\left[F_1(s)\right] = -\frac{s^2}{2}\frac{dp}{dx} + R_1(s), \tag{158}$$

$$\frac{d}{dx}\left[F_2(s)\right] = -\frac{1-s^2}{2}\frac{dp}{dx} + R_2(s). \tag{159}$$

This provides two equations from which to determine both the free boundary $s(x)$ and the pressure gradient. Elimination of dp/dx between (158) and (159) leads to a first-order o.d.e. for $s(x)$ whose solution, with $s(0) = 0$ is

$$x = \int_0^s I(s')\,ds', \quad \text{where} \quad I(s) = \frac{(1-s^2)F_1'(s) - s^2F_2'(s)}{(1-s^2)R_1(s) - s^2R_2(s)}, \tag{160}$$

that is

$$I(s) = ns\left\{(1-s^2)^3\left[40 - 130s^2 + 101s^4 + 7s^6 + n\left(-60 + 185s^2 - 143s^4\right)\right]\right.$$

$$+(1-s^2)^2\log s\left[2\left(60 - 155s^2 + 17s^4 + 125s^6 - 5s^8\right)\right.$$

$$\left.+n\left(-140 + 275s^2 + 140s^4 - 359s^6\right)\right]$$

$$+2(1-s^2)\log^2 s\left[2\left(30 - 55s^2 - 56s^4 + 92s^6 + 21s^8 - 2s^{10}\right)\right.$$

$$+n\left(-30-55s^2+299s^4-121s^6-153s^8\right)\Big]$$

$$+4\log^3 s\left[-2\left(5-5s^2-19s^4+15s^6+10s^8\right)\right.$$

$$+n\left(-15+70s^2-47s^4-108s^6+94s^8+18s^{10}\right)\Big]$$

$$+8n\log^4 s\left[5-5s^2-19s^4+15s^6+10s^8\right]\Big\}\Big/$$

$$\left\{48(1-s^2)(1+\log s-s^2)\left[(1-s^2)(2-n-s^2)+(2+n-3ns^2)\log s+2n\log^2 s\right]\right\}. \tag{161}$$

Some idea of the qualitative behaviour of the complicated expression (161) may be obtained by examining its asymptotic behaviour. When s is small,

$$I(s)\sim\frac{5ns\,(2n\log s+2-3n)}{12\,(2n\log s-n+2)^2}\quad\text{as}\quad s\to 0,$$

or, if $s=\epsilon\sigma$, then

$$I(\epsilon\sigma)\sim\frac{5\epsilon\sigma\,(2\log\sigma-3)}{12\,(2\log\sigma-1)^2},$$

which clearly matches with the large-σ expansion (152) of our entry-region approximation.

On the other hand, as s approaches its maximum value r_*, I blows up like

$$I(s)\sim\left\{\frac{r_*^2 n\left[(5+5r_*^2-4r_*^4)-n(15-13r_*^2+4r_*^4)\right]}{48(1-n)^2}\right\}\frac{1}{r_*-s}.$$

If we substitute in the approximate value of r_*, we find that

$$I(s)\sim\left\{\frac{0.02477n(1-2.1405n)}{(1-n)^2}\right\}\frac{1}{r_*-s}. \tag{162}$$

Since n is supposed to be a small parameter, we see that the coefficient in braces is a numerically small constant. Thus, as shown in figure 11, $I(s)$ remains small until s is very close to r_*, where it rapidly blows up. This means that the boundary layer grows quickly, not noticing the weak return flow until it is very close to the fully-developed profile. The behaviour of $s(x)$ corresponding to (162) is

$$s\sim r_*-\text{const}\,\exp\left(\frac{-(1-n)^2x}{0.02477n(1-2.1405n)}\right)\quad\text{as}\quad x\to\infty.$$

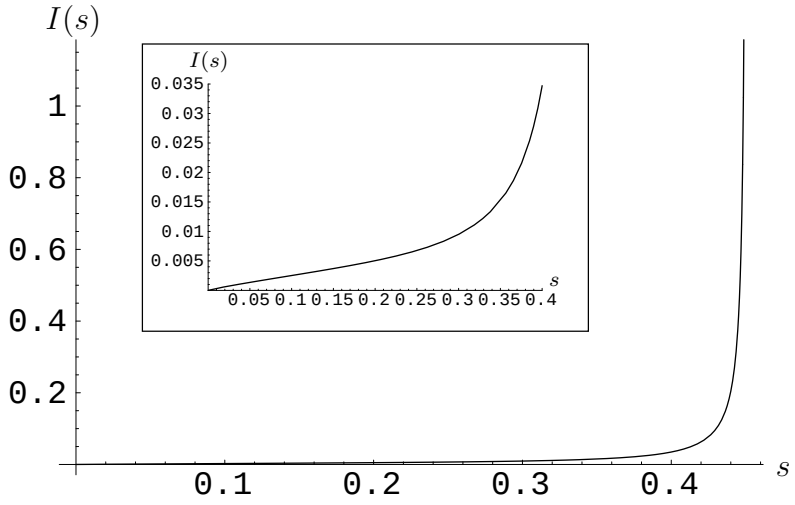

Figure 11: The integrand $I(s)$ defined by (161) for $n = 0.1$; the inset shows the behaviour at small s.

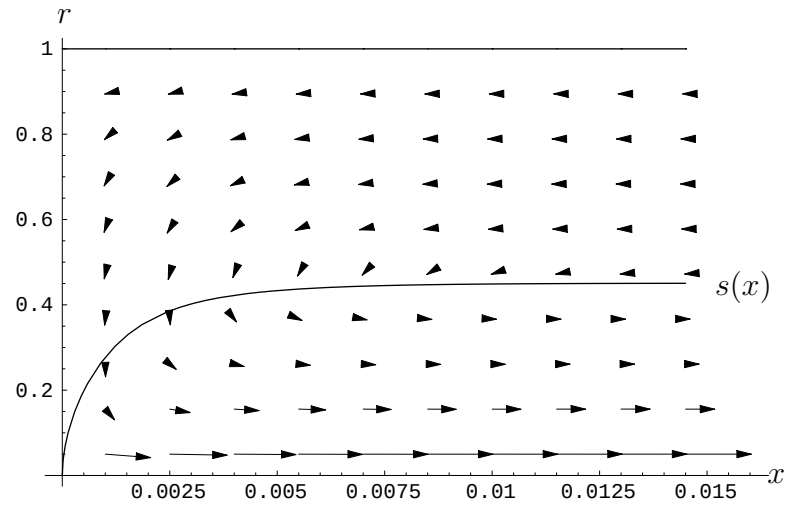

Figure 12: The boundary layer edge $s = s(x)$, the flow in the boundary layer and the return flow outside; $n = 0.1$.

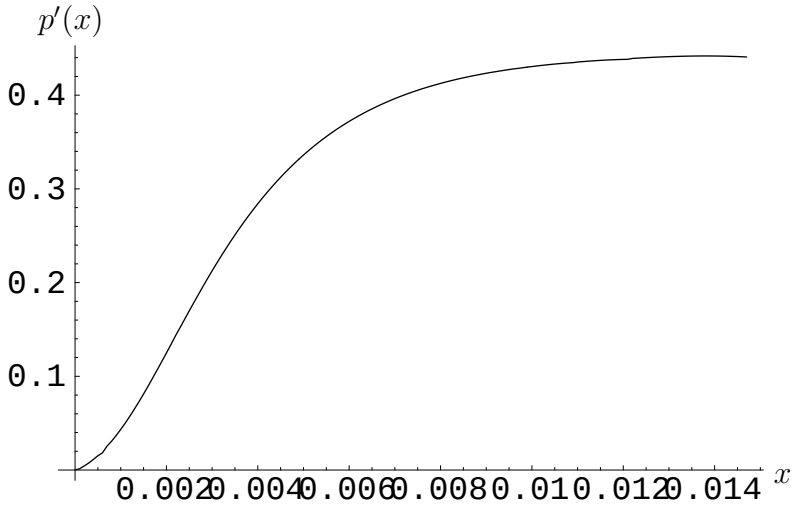

Figure 13: The pressure gradient $p'(x)$ in the developing flow; $n = 0.1$.

The boundary-layer thickness, determined by performing the integral (160) numerically, is plotted in figure 12 along with the flow field. As predicted, the boundary layer develops over a very small distance, while the flow converges rapidly to the fully-developed profile. The velocity decays sharply away from the singularity at $r = 0$ and the return flow is everywhere relatively weak. The corresponding pressure gradient is shown in figure 13. The pressure gradient is initially zero, as assumed in the entry region and, like the velocity field, evolves rapidly towards its constant fully-developed value

$$p'(\infty) = \frac{4n}{1-n} = \frac{4}{9} \quad \text{when} \quad n = 0.1.$$

5 Summary and Suggestions for Future Work

In this report, we have developed a mathematical theory to describe the flow of a drawn glass fiber and the air flow near to it. We have presented equations and formulas which indicate how these flows depend on the physical parameters characterizing the glass drawing process. Further analysis of this information could help inform ways of improving the glass fiber drawing process.

For example, further examination, such as a stability analysis, of the equations in §2 describing the flow of the glass could be useful in determining physical parameter ranges for which the glass fiber would be more likely to adopt a uniform cross section. Also, the development of a quantitative description of the air flow near the fiber in §3 and §4 could be used as an ingredient in a study of the rate at which the glass fiber cools as it stretches. There are however, several steps which would need to be taken before the theory would be practical at this level.

First, because of the rather large Reynolds number near the thinnest part of the fiber, we should consider whether turbulence modifies the boundary layer structure [3, 9]. Secondly, the strong temperature gradients between the hot fiber (near 1500 K) and the surrounding air (300 K) will likely imply that the heat flux will modify the velocity field. The heat flux itself is of course influenced by the convective effects of the boundary layer. This leads to a difficult coupled nonlinear problem. Likely some large-scale numerical computations will be necessary to resolve such a problem. Our intention here is merely to get some basic understanding of how the geometry of the fiber-drawing process would affect the air flow near the flowing fiber.

References

[1] C.-H. Chen. Mixed convection cooling of a heated, continuously stretching surface. *Heat and Mass Transfer*, 36:79–86, 2000.

[2] Harold R. Clark and Montri Viriyayuthakorn. The VAD preform stretching process: A numerical model for evaluation of internal distortion. *Journal of Lightwave Technology*, LT-4(8):1039–1047, August 1986.

[3] J. Cousteix. Three-dimensional and unsteady boundary-layer computations. In *Annual review of fluid mechanics, Vol. 18*, pages 173–196. Annual Reviews, Palo Alto, CA, 1986.

[4] George Emanuel. *Analytical Fluid Dynamics: Second Edition*, part V. CRC Publishers, Boca Raton, FL, second edition, 2001.

[5] Joseph B. Keller and Michael J. Ward. Asymptotics beyond all orders for a low Reynolds number flow. *J. Engrg. Math.*, 30(1-2):253–265, 1996. The centenary of a paper on slow viscous flow by the physicist H. A. Lorentz.

[6] M. C. A. Kropinski, Michael J. Ward, and Joseph B. Keller. A hybrid asymptotic-numerical method for low Reynolds number flows past a cylindrical body. *SIAM J. Appl. Math.*, 55(6):1484–1510, 1995.

[7] Franklin K. Moore. Three-dimensional boundary layer theory. In H. L. Dryden and Th. von Kármán, editors, *Advances in Applied Mechanics*, volume IV, pages 159–228. Academic Press, New York, 1956.

[8] U. C. Paek and R. B. Runk. Physical behavior of the neck-down region during furnace drawing of silica fibers. *J. Appl. Physics*, 49(8):4417–4422, August 1978.

[9] B. C. Sakiadis. Boundary-layer behavior on continuous solid surfaces: III. The boundary layer on a continous cylindrical surface. *A. I. Ch. E. Journal*, 7(3):467–472, September 1961.

[10] Steven H. Strogatz. *Nonlinear Dynamics and Chaos*, chapter 6. Addison-Wesley, Reading, MA, USA, 1994.

[11] Matthew Sweetland and John H. Lienard V. Evaporative cooling of continuously drawn glass fibers by water sprays. *Int. J. Heat Mass Transfer*, 43:777–790, 2000.

[12] Michael J. Ward, William D. Henshaw, and Joseph B. Keller. Summing logarithmic expansions for singularly perturbed eigenvalue problems. *SIAM J. Appl. Math.*, 53(3):799–828, 1993.